

Heavy Color-Octet Particles at the LHC

Chien-Yi Chen¹, Ayres Freitas², Tao Han², and Keith S. M. Lee^{3,4}

¹ *Department of Physics, Brookhaven National Laboratory, Upton, NY 11973, USA*

² *PITTSburgh Particle physics, Astrophysics, and Cosmology Center (PITT PACC),
Department of Physics & Astronomy, Univ. of Pittsburgh, Pittsburgh, PA 15260, USA*

³ *Perimeter Institute for Theoretical Physics, Waterloo, ON Canada N2L 2Y5*

⁴ *Department of Physics & Astronomy, Univ. of Waterloo, Waterloo, ON Canada N2L 3G1*

Abstract

Many new-physics models, especially those with a color-triplet top-quark partner, contain a heavy color-octet state. The “naturalness” argument for a light Higgs boson requires that the color-octet state be not much heavier than a TeV, and thus it can be pair-produced with large cross sections at high-energy hadron colliders. It may decay preferentially to a top quark plus a top-partner, which subsequently decays to a top quark plus a color-singlet state. This singlet can serve as a WIMP dark-matter candidate. Such decay chains lead to a spectacular signal of four top quarks plus missing energy. We pursue a general categorization of the color-octet states and their decay products according to their spin and gauge quantum numbers. We review the current bounds on the new states at the LHC and study the expected discovery reach at the 8-TeV and 14-TeV runs. We also present the production rates at a future 100-TeV hadron collider, where the cross sections will be many orders of magnitude greater than at the 14-TeV LHC. Furthermore, we explore the extent to which one can determine the color octet’s mass, spin, and chiral couplings. Finally, we propose a test to determine whether the fermionic color octet is a Majorana particle.

1 Introduction

The historic discovery of the Higgs boson has led particle physics to an interesting juncture. On the one hand, for the first time in history, we have a consistent relativistic quantum-mechanical model, the Standard Model (SM), that is valid all the way up to the Planck scale. On the other hand, there remain many unanswered theoretical and observational questions, which imply the need for physics beyond the SM. The putative “naturalness” of a light Higgs boson is arguably a strong indication of new physics near the TeV scale, and a top-quark partner is eagerly anticipated as a cure for the quadratic sensitivity of the Higgs mass to the new-physics scale.

Besides the color-triplet top-quark partner, many new-physics models also contain a heavy color-octet state. The naturalness argument requires the color-octet state to be not much heavier than the TeV scale [1], which should be accessible at LHC energies (for a recent account, see for example Ref. [2] and references therein). Examples of electrically neutral color-octet particles include the gluino in supersymmetry [3], techni-rhos [4] or top-gluons [5] in models with strong TeV-scale dynamics, and Kaluza-Klein (KK) gluons in models with universal extra dimensions [6]. For large regions of parameter space in these models, the color-octet particles decay preferentially to a top quark plus a heavy top-quark partner, either owing to large couplings between the color octet and the top-quark partner or because other new particles are very massive and thus effectively decoupled. The top partner subsequently decays to a top quark plus a color-singlet state. These decay chains lead to a spectacular signal of four top quarks plus missing energy.

In this paper, we model-independently study processes of the form

$$pp \rightarrow \mathcal{Z} \bar{\mathcal{Z}} \rightarrow t \bar{t} Y \bar{Y} \rightarrow t \bar{t} t \bar{t} X \bar{X}, \quad (1)$$

where \mathcal{Z} is a new color-octet particle, Y a new color-triplet particle (top partner), and X a color singlet. The electrically neutral X is assumed to be stable and thus could be a dark-matter candidate, which would manifest itself as missing energy in a collider experiment. For all new particles in this process (X , Y and \mathcal{Z}), we consider different spin assignments (0, 1/2 and 1). We also distinguish the possibility that the color octet may or may not be its own antiparticle ($\mathcal{Z} = \bar{\mathcal{Z}}$ or $\mathcal{Z} \neq \bar{\mathcal{Z}}$). Each combination is exemplified by particles in well-motivated new-physics models. For example, \mathcal{Z} could be the gluino, Y a scalar top, and X the lightest neutralino in the Minimal Supersymmetric Standard Model (MSSM). This case has been studied extensively (see, for example, Refs. [2, 7–14]). Vector (scalar) X and \mathcal{Z} particles appear in models with at least one (at least two) universal extra dimension(s) [6], stemming from the KK excitations of the multidimensional gauge-boson fields. Spin-0 color singlets and octets are also found in $\mathcal{N} = 2$ supersymmetry (SUSY) [15–17]. Fermionic and vector top partners, Y , exist in extra-dimensional models [6] and SUSY models with an extended gauge sector [18]. However, instead of focusing on specific particles in a particular model, we pursue a general categorization in this paper, assuming only a discrete symmetry that ensures the stability of X .

Color octets with $\mathcal{O}(\text{TeV})$ masses can be pair produced with large cross sections at the LHC. Consequently, within the framework of the MSSM, the ATLAS and CMS collaborations

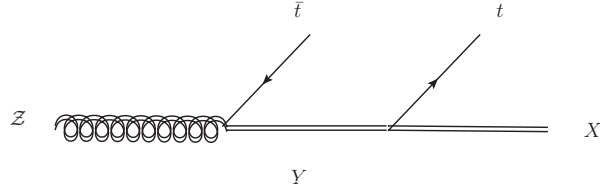


Figure 1: The decay chain of \mathcal{Z} to the color singlet X via the color triplet Y . Double lines denote new particles, while single lines denote SM particles. If \mathcal{Z} is a self-conjugate field, this decay chain is accompanied by the charge-conjugate version $\mathcal{Z} \rightarrow t\bar{Y} \rightarrow t\bar{t}X$.

have put strong bounds on their parameter space [7–11]. In this paper, we recast these limits for different spin assignments of the new particles. Despite these bounds, we show that the full-energy run of the LHC (with 13–14 TeV collision energy) will have a significantly expanded potential for searching for and possibly discovering a signature of the type in Eq. (1). If a signal is observed, the next goal will be the determination of the spins and couplings of the new particles, \mathcal{Z} , Y and X . We study several observables for this purpose and demonstrate their usefulness with numerical Monte Carlo simulation. To avoid ambiguities due to model-dependent branching fractions, we do not rely on the total cross section in this set of variables. Looking further ahead, we also present the cross sections at the 100-TeV VLHC, where the signal production rates can be several orders of magnitude greater than the 14-TeV expectations and thus extend the discovery range substantially.

This paper is organized as follows. After introducing the model-independent classification of gluon and top partners and discussing their production and decay in section 2, we show the current bounds and future reach of the LHC in sections 3 and 4, respectively. Section 5 is devoted to the determination of the masses, spins and couplings of the new particles from LHC data. Finally, conclusions are presented in section 6.

2 General Framework

In the following, we study the phenomenology of the Standard Model extended by three new particles: a neutral color singlet X , a color triplet Y (and its antiparticle \bar{Y}) with charge $+2/3$ ($-2/3$), and a color octet \mathcal{Z} . All new particles are assumed to be charged under some new global symmetry, so that they can be produced only in pairs and their decay chains end with the lightest new particle, which, because of astrophysical limits, must be the X . Searches for gluinos by ATLAS and CMS [7–11] have led to strong lower bounds on the mass of the \mathcal{Z} , so it is reasonable to assume the mass hierarchy $m_{\mathcal{Z}} > m_Y > m_X$, leading to the decay chain shown in Fig. 1.

When one demands gauge invariance and renormalizability, there are four possible spin combinations (with spin 0, 1/2 and 1) allowing a coupling between Y , X and t , and four combinations for a coupling between \mathcal{Z} , Y and t . We summarize the possible combinations in Table 1. The top panel of the table (cases i–iv) reproduces the color-triplet interactions constructed in Ref. [19]. These form the basis for our current extended theoretical framework

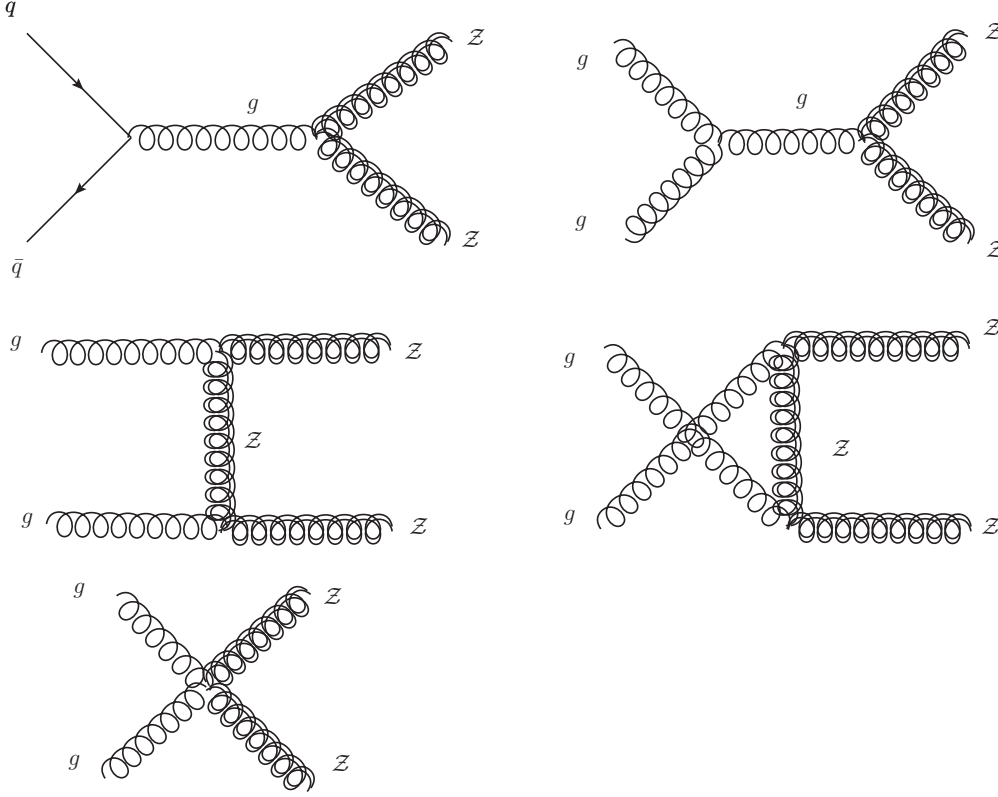


Figure 2: Leading-order diagrams for the pair production of the color octet \mathcal{Z} at hadron colliders. Double lines denote new particles, while single lines denote SM particles. The last diagram exists only for a bosonic \mathcal{Z} .

including the color octet \mathcal{Z} (cases v–viii). By default, the X and \mathcal{Z} are assumed to be self-conjugate, but we also explore the phenomenological differences between the cases where \mathcal{Z} is a Majorana fermion (case vi(a)) and a Dirac fermion (case vi(b)), denoted \mathcal{Z}_D , which can arise in models with $\mathcal{N} = 2$ supersymmetry [16]. Also shown in the table are the structure of the relevant couplings and examples for concrete realizations of each case in a specific model. For fermions, we allow a general chirality structure, specified by the parameters $a_{L,R}$ and $b_{L,R}$.

Direct production of $Y\bar{Y}$ pairs was discussed in detail in Ref. [19]. Here we consider pair production of \mathcal{Z} particles, which subsequently decay according to the decay chain in Fig. 1. They can be produced with sizeable cross sections at the LHC, even for large masses, $m_{\mathcal{Z}} > 1$ TeV, and lead to a distinct final state of four top quarks and missing energy. The dominant modes for \mathcal{Z} pair production at hadron colliders are the QCD subprocesses

$$q\bar{q}, gg \rightarrow \mathcal{Z}\bar{\mathcal{Z}}, \quad (2)$$

which are described at leading order by the diagrams in Fig. 2. The form of the gluon- \mathcal{Z} vertex is dictated by QCD gauge invariance and shown in Table 1.

	Y $s, I_{\text{SU}(3)}$	X $s, I_{\text{SU}(3)}$	$GY\bar{Y}$ coupling	XYt coupling	sample model and decay $Y \rightarrow tX$
i	0, 3	$\frac{1}{2}, \mathbf{1}$	$G^{a\mu} Y^* \overleftrightarrow{\partial}_\mu T^a Y$	$\bar{X} \Gamma t Y^*$	MSSM $\tilde{t} \rightarrow t \tilde{\chi}_1^0$
ii	$\frac{1}{2}, \mathbf{3}$	0, 1	$\bar{Y} \mathcal{G}^a T^a Y$	$\bar{Y} \Gamma t X$	UED $t_{\text{KK}} \rightarrow t \gamma_{H,\text{KK}}$
iii	$\frac{1}{2}, \mathbf{3}$	1, 1	$\bar{Y} \mathcal{G}^a T^a Y$	$\bar{Y} \not{X} \Gamma t$	UED $t_{\text{KK}} \rightarrow t \gamma_{\text{KK}}$
iv	1, 3	$\frac{1}{2}, \mathbf{1}$	$S_3[G, Y, Y^*]$	$\bar{X} \not{Y}^* \Gamma t$	[18] $\vec{Q} \rightarrow t \tilde{\chi}_1^0$

	\mathcal{Z} $s, I_{\text{SU}(3)}$	Y $s, I_{\text{SU}(3)}$	$G\mathcal{Z}\mathcal{Z}$ coupling	$\mathcal{Z}Yt$ coupling	sample model and decay $\mathcal{Z} \rightarrow Y\bar{t}$
v	0, 8	$\frac{1}{2}, \mathbf{3}$	$G^{a\mu} \mathcal{Z}^c \overleftrightarrow{\partial}_\mu \mathcal{Z}^b f^{abc}$	$\bar{Y} T^a \Gamma' t \mathcal{Z}^a$	UED $g_H \rightarrow t_{\text{KK}} \bar{t}$
vi(a)	$\frac{1}{2}, \mathbf{8}$	0, 3	$\bar{\mathcal{Z}}^c \mathcal{G}^a \mathcal{Z}^b f^{abc}$	$\bar{\mathcal{Z}}^a Y^* T^a \Gamma' t$	MSSM $\tilde{g} \rightarrow \tilde{t} \bar{t}$
vi(b)	$\frac{1}{2}, \mathbf{8}$	0, 3	$\bar{\mathcal{Z}}_D^c \mathcal{G}^a \mathcal{Z}_D^b f^{abc}$	$(\bar{\mathcal{Z}}_D^a)^* Y^* T^a b_L t_L + \bar{\mathcal{Z}}_D^a Y^* T^a b_R t_R$	$\mathcal{N} = 2$ SUSY $\tilde{g}_D \rightarrow \tilde{t} \bar{t}$
vii	$\frac{1}{2}, \mathbf{8}$	1, 3	$\bar{\mathcal{Z}}^c \mathcal{G}^a \mathcal{Z}^b f^{abc}$	$\bar{\mathcal{Z}}^a \not{Y}^* T^a \Gamma' t$	[18] $\tilde{g} \rightarrow \vec{Q} \bar{t}$
viii	1, 8	$\frac{1}{2}, \mathbf{3}$	$S_8[G, \mathcal{Z}, \mathcal{Z}]$	$\bar{Y} \not{\mathcal{Z}}^a T^a \Gamma' t$	UED $g_{\text{KK}} \rightarrow t_{\text{KK}} \bar{t}$

$$\Gamma \equiv a_L P_L + a_R P_R, \quad \Gamma' \equiv b_L P_L + b_R P_R$$

$$A \overleftrightarrow{\partial}_\mu B \equiv A(\partial_\mu B) - (\partial_\mu A)B$$

$$S_3[G, Y, Y^*] \equiv G_\mu^a Y_\nu^* \overleftrightarrow{\partial}^\mu T^a Y^\nu + G_\mu^a Y^{\mu*} \overleftrightarrow{\partial}^\nu T^a Y_\nu - G_\mu^a Y_\nu^* \overleftrightarrow{\partial}^\nu T^a Y^\mu$$

$$S_8[G, \mathcal{Z}, \mathcal{Z}^*] \equiv f^{abc} \left[G_\mu^a \mathcal{Z}_\nu^{c*} \overleftrightarrow{\partial}^\mu \mathcal{Z}^{b\nu} + \mathcal{Z}_\mu^b G_\nu^a \overleftrightarrow{\partial}^\mu \mathcal{Z}^{c\nu*} + \mathcal{Z}_\mu^{c*} \mathcal{Z}_\nu^b \overleftrightarrow{\partial}^\mu G^{a\nu} \right]$$

Table 1: Quantum numbers and couplings of the new particles, X , Y and \mathcal{Z} , which interact with the SM top quark, t . In the last column, \tilde{g} , \tilde{t} and $\tilde{\chi}_1^0$ are the gluino, the scalar top and lightest neutralino in the MSSM, respectively [3]. g_{KK} , t_{KK} , γ_{KK} , g_H and $\gamma_{H,\text{KK}}$ are the first-level Kaluza-Klein excitations of the gluon, the top, the photon, and an extra-dimensional component of a gluon and a photon, respectively, in universal extra dimensions (UED) [6]. \tilde{g}_D denotes a Dirac gluino in $\mathcal{N} = 2$ supersymmetry [16, 20]. Finally, \vec{Q} is the vector superpartner in a supersymmetric model with an extended gauge sector [18].

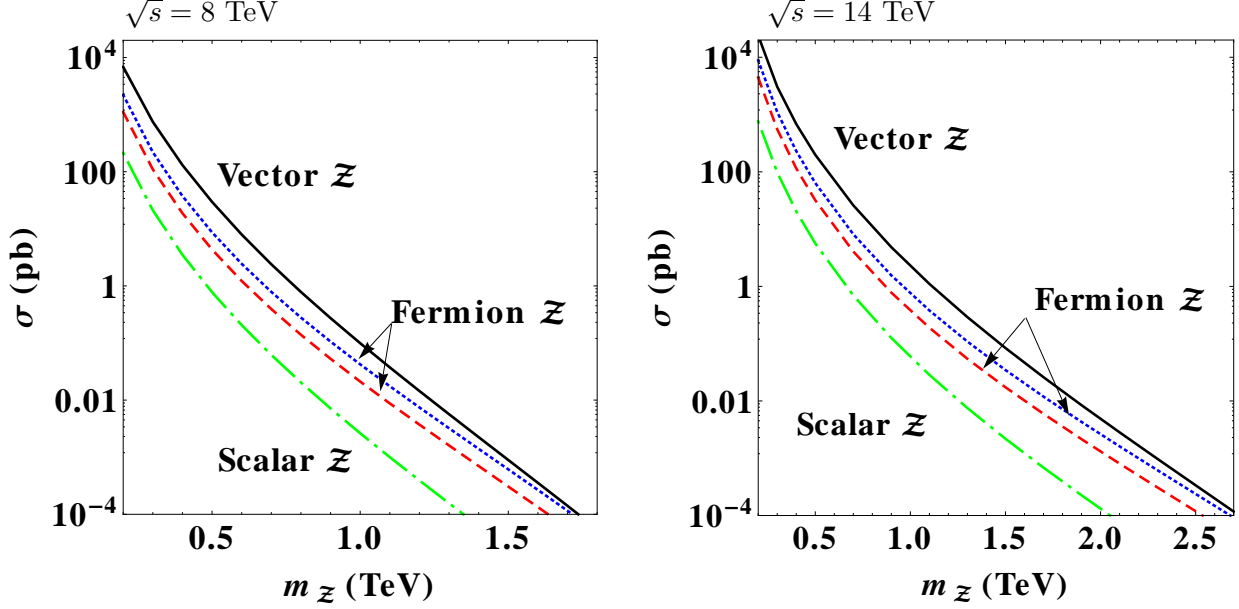


Figure 3: Production cross sections for $pp \rightarrow Z\bar{Z}$ at the LHC for 8 TeV (left) and 14 TeV (right), as a function of the mass m_Z , for a vector Z (black solid), Dirac Z (blue dotted), Majorana Z (red dashed), and scalar Z (green dot-dashed).

For the different Z spin assignments, the total QCD cross sections at the LHC are shown in Fig. 3 as a function of m_Z . The values include next-to-leading-order (NLO) QCD corrections for the scalar Z [21], and NLO and next-to-next-to-leading logarithmic (NNLL) corrections for the Majorana fermion Z [22], with extrapolation to larger or smaller values of m_Z where necessary. For pair production of color-octet Dirac fermions and vectors, the QCD corrections have not been calculated to the best of our knowledge. Therefore, we simply assume that the K -factor for Dirac fermions is identical to the one for Majorana fermions, and that the K -factor for the spin-1 case is the same as for the scalar case, since scalars and vectors share the same diagrams.

As Fig. 3 shows, the cross section for fermion Z pairs is about one order of magnitude larger than for the scalar case, because of the fermion's larger number of spin degrees of freedom and p -wave suppression of the scalar. The latter effect is most pronounced near threshold, where the p -wave production has a velocity dependence of $\sigma \sim \beta^3 = (1 - 4m_Z^2/\hat{s})^{3/2}$, whereas an s -wave leads to $\sigma \sim \beta$. As a result, the difference between the scalar and fermion cross sections increases at small values of β , that is, for large values of m_Z . The production cross section for Dirac fermions is twice as large as for Majorana fermions, since Dirac fermions have twice the number of independent degrees of freedom. The production rate for a vector Z is larger than that for Majorana fermions by another factor of about five.

For illustration, Fig. 4(a) shows the total production cross sections for $Z\bar{Z}$ pairs at a proposed 100-TeV collider. We approximate the K -factors for scalar and vector $Z\bar{Z}$ production at $\sqrt{s} = 100$ TeV by assuming the same energy dependence as for the fermionic case, that is, we multiply their K -factors at $\sqrt{s} = 14$ TeV by the ratio of the fermionic

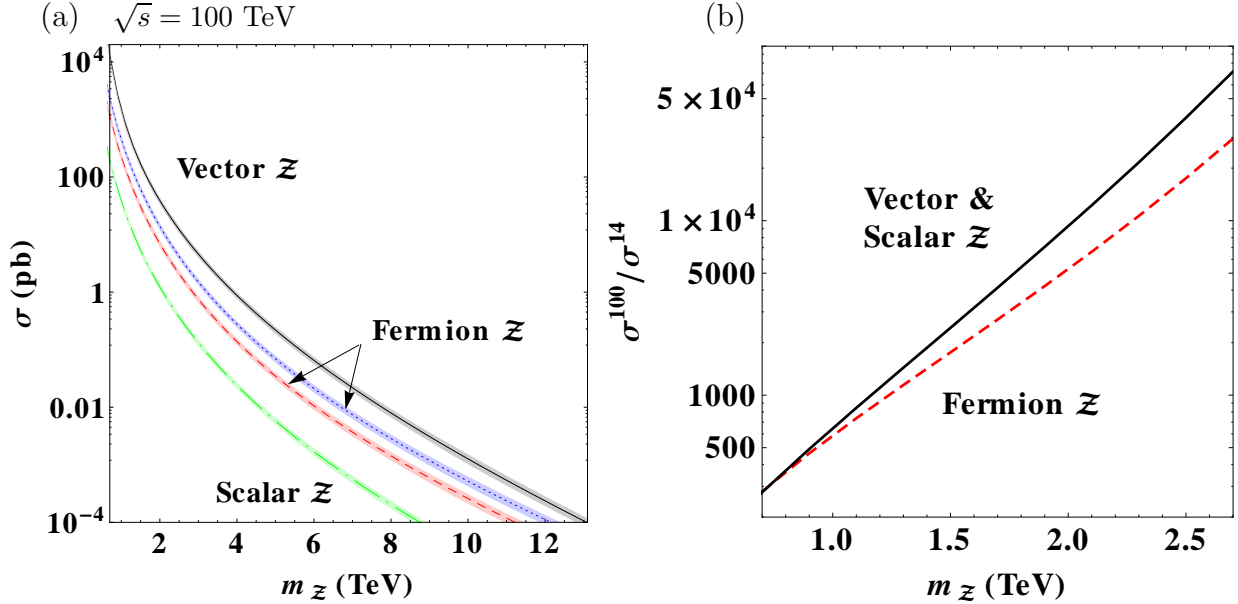


Figure 4: (a) Production cross sections for $pp \rightarrow Z\bar{Z}$ at a pp collider with $\sqrt{s} = 100$ TeV and (b) the cross-section ratios $\sigma(100 \text{ TeV})/\sigma(14 \text{ TeV})$, as a function of the mass m_Z , for a vector Z (black solid), Dirac Z (blue dotted), Majorana Z (red dashed), and scalar Z (green dot-dashed). The widths of the bands indicate the estimated theoretical uncertainty [23].

K -factors at 100 TeV [23] and 14 TeV. The shaded bands underlying each curve indicate the estimated theoretical uncertainty due to parton distribution functions and the dependence on renormalization and factorization scales, as estimated in Ref. [23]. For comparison with the LHC reach, we show the cross-section ratios at the two energies, $\sigma(100 \text{ TeV})/\sigma(14 \text{ TeV})$, in Fig. 4(b). We see that the production cross sections for the color-octet particles could increase by a factor of 500–50,000 for a mass of 1–2.5 TeV. Thus, color octets with masses of $\mathcal{O}(10 \text{ TeV})$ will become accessible at such a machine, which will reach a cross section of order 0.1–1 fb. However, in the following sections, we shall focus on the LHC phenomenology of these particles.

3 Current Bounds from the 8-TeV LHC

Processes of the form (1) can be probed through LHC searches for gluino production with the dominant decay $\tilde{g} \rightarrow t\bar{t}\tilde{\chi}_1^0$, where $\tilde{\chi}_1^0$ is the lightest neutralino. In fact, the scenario vi(a)+i in Table 1 corresponds exactly to this MSSM process. For the other cases in Table 1, one can obtain limits by recasting the experimental MSSM results [7–11]. Some of the strongest constraints are obtained from searches for multi-jet final states [9, 11]. Here, we instead focus on searches with two same-sign leptons in the final state [7, 8, 10], which have a slightly smaller mass reach but significantly less SM background. The reduced background is an important advantage for model discrimination, which will be discussed in section 5. In particular, we adopt the ATLAS analysis from Ref. [7], but the more recent paper [8] and

the CMS analysis in Ref. [10] lead to similar limits.

We have reproduced the simulation of the MSSM signal in Ref. [7] using PYTHIA 6.4 [24] and employing the selection cut sets SR1b and SR3b from that analysis. Explicitly, these cuts are defined as follows:

$$\begin{aligned} \text{Pre-sel.: } & \text{Two leptons with } p_{T,\ell} > 20 \text{ GeV, } |\eta_e| < 2.47, |\eta_\mu| < 2.4, \text{ and same charge,} \\ & N_j \text{ jets with } p_{T,j} > 40 \text{ GeV, } |\eta_j| < 2.8, \\ & N_b \text{ } b\text{-jets with 70\% } b\text{-tagging efficiency and 1\% light-jet mis-tagging rate,} \\ & \Delta R_{\ell\ell} > 0.3, \quad \Delta R_{jj} > 0.4, \quad \Delta R_{\ell j} > 0.3. \end{aligned} \quad (3)$$

$$\begin{aligned} \text{SR1b: } & N_j \geq 3, \quad N_b \geq 1, \\ & |\not{\mathbf{p}}_T| > 150 \text{ GeV, } M_T(\ell_1, \not{\mathbf{p}}_T) > 100 \text{ GeV, } m_{\text{eff}} > 700 \text{ GeV.} \end{aligned} \quad (4)$$

$$\text{SR3b: } N_j \geq 4, \quad N_b \geq 3. \quad (5)$$

Here, p_T and η denote the transverse momentum and pseudorapidity of an object, respectively, $\Delta R_{ab} \equiv \sqrt{(\eta_a - \eta_b)^2 + (\phi_a - \phi_b)^2}$, and $\not{\mathbf{p}}_T$ is the missing transverse momentum. The number N_j includes both light jets and b -jets. The effective mass $m_{\text{eff}} = \sum_\ell |\mathbf{p}_{T,\ell}| + \sum_j |\mathbf{p}_{T,j}| + |\not{\mathbf{p}}_T|$ is the scalar sum of the missing transverse momentum and the transverse momenta of the selected leptons and jets, and $M_T(\ell_1, \not{\mathbf{p}}_T) = \sqrt{2|\mathbf{p}_{T,\ell_1}||\not{\mathbf{p}}_T| - 2\mathbf{p}_{T,\ell_1} \cdot \not{\mathbf{p}}_T}$ is the transverse mass associated with the leading lepton ℓ_1 . A cut on M_T reduces the background from gauge-boson pair production.

After applying these cuts for $\sqrt{s} = 8$ TeV, we obtain event numbers that are very similar to those in Table 5 of Ref. [7] (for an MSSM signal using the same gluino, stop and neutralino masses as therein).

The accurate evaluation of the SM backgrounds depends additionally on issues like particle (mis)identification efficiencies; for these, we simply take the numbers from Table 3 in Ref. [7]. We then combine the SM backgrounds with our simulation of the signal, for the case of the MSSM, which corresponds to scenario vi(a)+i in Table 1 (that is, the fermion-scalar-fermion spin combination), and perform a χ^2 analysis. The results for $\sqrt{s} = 8$ TeV are shown in the left panel of Fig. 5, as a function of m_Z and m_X , with $m_Y = (m_Z + m_X)/2$.

As Fig. 5 shows, fermionic octets (gluinos) decaying into top-quark final states are excluded for $m_Z \lesssim 1160$ GeV. This limit approximately agrees with Ref. [7], although the detailed extent of the excluded region depends on the choice of m_Y .

4 Signal Observability at the 14-TeV LHC

To obtain projections for $\sqrt{s} = 14$ TeV, we adjust the selection cuts in Eqs. (3)–(5) to obtain roughly the same signal efficiency as for $\sqrt{s} = 8$ TeV. Specifically, all cuts on dimensionless variables are left unchanged, while the cut values for dimensionful variables are scaled up by a factor of 1.1. We assume that, with this rescaled set of cuts, the same percentage of SM background events is retained as at $\sqrt{s} = 8$ TeV with the original set of cuts, Eqs. (3)–(5). In other words, we estimate the SM background by scaling the event numbers from Ref. [7] by

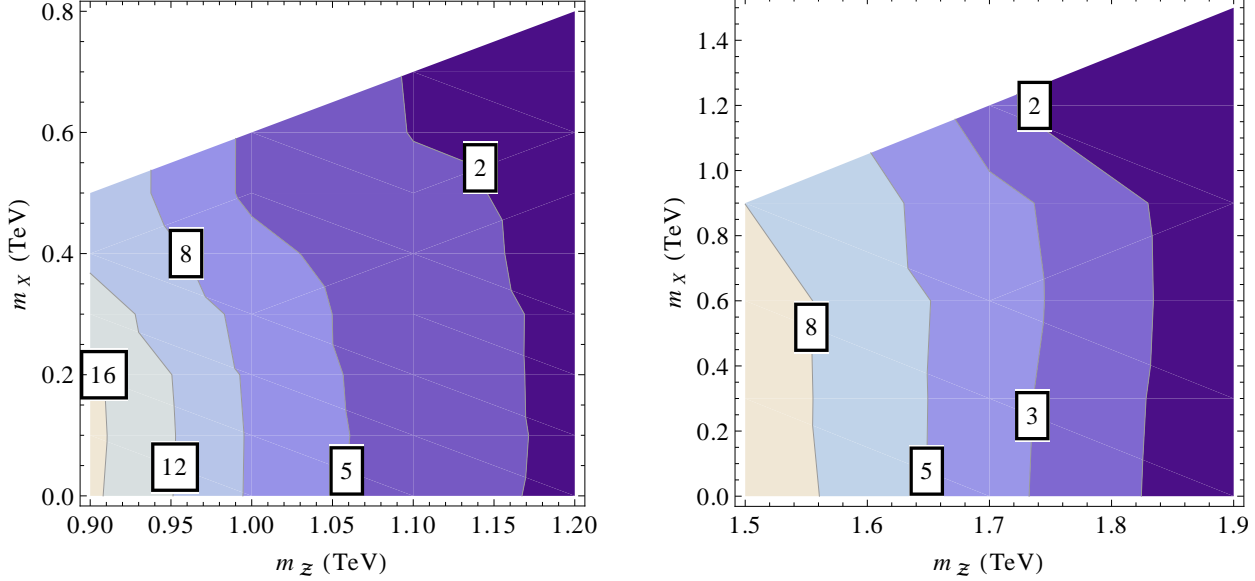


Figure 5: Exclusion limits and projected discovery reach for $pp \rightarrow \mathcal{Z}\bar{\mathcal{Z}} \rightarrow t\bar{t}Y\bar{Y} \rightarrow t\bar{t}t\bar{t}X\bar{X}$ when \mathcal{Z} is fermionic, as a function of the masses of \mathcal{Z} and X , with $m_Y = (m_{\mathcal{Z}} + m_X)/2$. The left panel corresponds to $\sqrt{s} = 8$ TeV and $\mathcal{L} = 21$ fb $^{-1}$, while the right panel corresponds to $\sqrt{s} = 14$ TeV and $\mathcal{L} = 300$ fb $^{-1}$. Contours are labeled with σ values indicating the statistical significance.

the ratio of the total cross sections for $\sqrt{s} = 14$ TeV and $\sqrt{s} = 8$ TeV. The cross sections for the dominant SM processes, $pp \rightarrow t\bar{t}W, t\bar{t}Z$ and $pp \rightarrow WZ, ZZ$, are taken from Refs. [25–27].

Using this procedure, we obtain the estimated reach of the 14-TeV LHC for the fermion-scalar-fermion spin combination given in the right panel of Fig. 5. Our results are consistent with Fig. 52 in Ref. [14], although in that reference a different set of cuts has been used and the scalar Y (stop) has been decoupled (that is, $m_Y \rightarrow \infty$).

The exclusion limits (for existing $\sqrt{s} = 8$ TeV data) and projected reach (for $\sqrt{s} = 14$ TeV) depend strongly on the spin of the \mathcal{Z} , because of its impact on the cross section $\sigma(pp \rightarrow \mathcal{Z}\bar{\mathcal{Z}})$. One can obtain approximate limits for scalar and vector \mathcal{Z} particles by rescaling the results in Fig. 5 by the relevant ratios of the cross sections shown in Fig. 3. Here, it is assumed that spin correlations in the decay chain $\mathcal{Z} \rightarrow t\bar{Y}/\bar{t}Y \rightarrow t\bar{t}X$ have a small effect on the experimental selection efficiency, so that they can be neglected. The results are shown in Fig. 6.

From Fig. 6, one can extract the approximate 2σ exclusion limits for scalar and vector \mathcal{Z} production at 8 TeV. For a light dark-matter candidate ($m_X \lesssim 200$ GeV), the bounds are shown in Table 2. The table also lists the expected reach of the 14-TeV run of the LHC for observation of the signal process in Eq. (1) at the 5σ level, again assuming a light dark-matter candidate ($m_X \lesssim 300$ GeV).

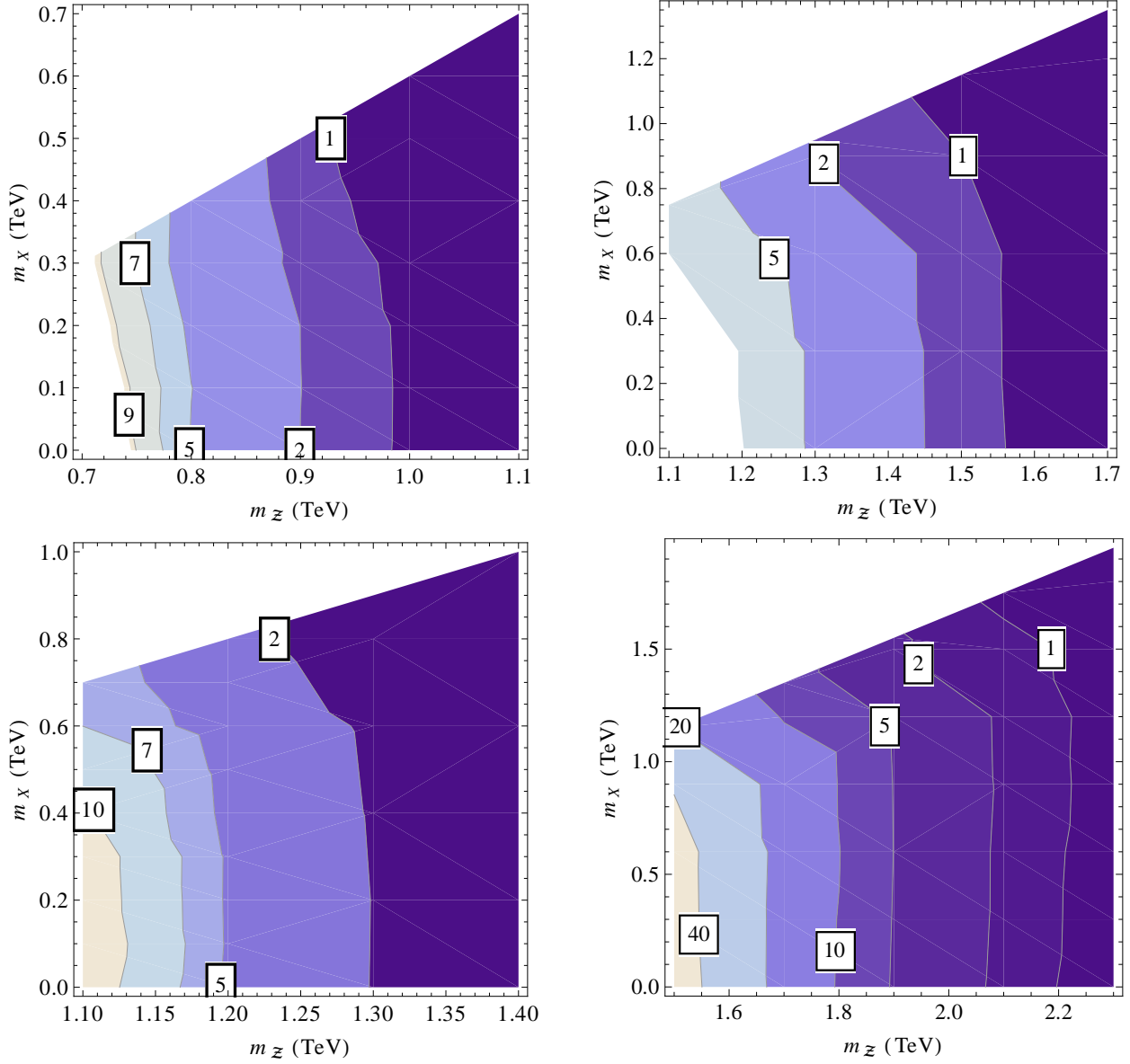


Figure 6: Exclusion limits and projected discovery reach for $pp \rightarrow Z\bar{Z} \rightarrow t\bar{t}Y\bar{Y} \rightarrow t\bar{t}t\bar{t}X\bar{X}$ for a scalar (upper) and a vector (lower) Z , as a function of the masses of Z and X , with $m_Y = (m_Z + m_X)/2$. The left panels correspond to $\sqrt{s} = 8$ TeV and $\mathcal{L} = 21$ fb $^{-1}$, while the right panels correspond to $\sqrt{s} = 14$ TeV and $\mathcal{L} = 300$ fb $^{-1}$. Contours are labeled with σ values indicating the statistical significance.

	spin-0 \mathcal{Z}	spin-1/2	spin-1
8 TeV (2σ with 21 fb^{-1})	900 GeV	1160 GeV	1290 GeV
14 TeV (5σ with 300 fb^{-1})	1280 GeV	1650 GeV	1900 GeV

Table 2: The 2σ exclusion limit at 8 TeV and 5σ discovery reach at 14 TeV for a spin-0, spin-1/2 and spin-1 \mathcal{Z} , assuming $m_X \lesssim 200$ (300) GeV for $\sqrt{s} = 8$ (14) TeV.

5 Determination of Model Properties

Once a new-physics signal consistent with the process in Eq. (1) has been observed at the LHC, it will be crucial to determine the particle properties in order to uncover the underlying theory. The kinematical distributions of the final-state particles can be used to determine the masses, spins and couplings of the X , Y and \mathcal{Z} particles. The analysis of direct pair production of the color triplet Y , $pp \rightarrow Y\bar{Y} \rightarrow t\bar{t}X\bar{X}$, can already yield valuable information about the properties of Y and the singlet X [19]. In this section, we shall instead be concerned primarily with the determination of the properties of the color octet \mathcal{Z} from the process (1).

As in the previous sections, we shall focus on the same-sign lepton signature, where each of the directly produced color octets decays through one leptonically and one hadronically decaying top quark, $\mathcal{Z}\bar{\mathcal{Z}} \rightarrow t_\ell t_\ell \bar{t}_h \bar{t}_h + \cancel{E}$ or $\mathcal{Z}\bar{\mathcal{Z}} \rightarrow \bar{t}_\ell \bar{t}_\ell t_h t_h + \cancel{E}$ (where \cancel{E} denotes missing transverse energy). Since this signal has small SM backgrounds, we shall neglect them in the following, in order to highlight more clearly the differences between the various scenarios in Table 1. Of course, in a detailed experimental or phenomenological analysis, the SM background contamination and its uncertainty will need to be accounted for, but we leave this for future work.

5.1 Masses

The distribution of the invariant mass, $m_{t\bar{t}}$, of the top-antitop pair from the decay chain $\mathcal{Z} \rightarrow t\bar{t}X$ (see Fig. 1) has a sharp endpoint at

$$(m_{t\bar{t}}^{\max})^2 = \frac{(m_{\mathcal{Z}}^2 - m_Y^2)(m_Y^2 - m_X^2)}{m_Y^2}. \quad (6)$$

Even if one of the top quarks decays leptonically, the invariant-mass distribution of the visible $t\bar{t}$ decay products ($b\bar{b}jj\ell$) still has the endpoint in Eq. (6), but with a shallower slope. In addition to measuring $m_{t\bar{t}}^{\max}$, one could obtain information about m_X and m_Y from the process $pp \rightarrow Y\bar{Y} \rightarrow t\bar{t}X\bar{X}$, using the observable M_{T2} or one of its variants [19, 28, 29]. By combining these observables, one could in principle determine m_X , m_Y and $m_{\mathcal{Z}}$ independently, albeit with poor precision.

If instead one focuses on the all-hadronic decay channel of the top quark, so that all top momenta can be reconstructed, one can take advantage of the kinematical method in Ref. [30], which gives relatively large errors in m_X but fairly good precision for $m_{\mathcal{Z}}$ and m_Y . However, the separation of the four top quarks in a given event is a difficult problem, which

may be aided by the use of a top-tagging algorithm (see, for example, Ref. [31]). Firmer conclusions will require a detailed simulation, which is beyond the scope of this paper.

5.2 Spin

For a decay chain of the form in Fig. 1, one can obtain information about the spins of the \mathcal{Z} , Y , and X particles from spin-correlation effects, which are reflected in the shape of the $t\bar{t}$ invariant-mass distribution. This strategy has been studied extensively for similar decay chains involving leptons instead of top quarks [32–34]. In contrast to these studies, one must account for the non-negligible mass of the top quark. Secondly, in focusing on the same-sign lepton signature, one cannot fully reconstruct the $t\bar{t}$ mass because of the missing neutrino from the leptonic top decay. Instead, one has to work with the visible decay products of each decay chain, that is, two b jets, two light jets, and one charged lepton $\ell = e, \mu$. The invariant mass of these objects, $m_{bbjj\ell}$, will have a distribution with similar qualitative features to the $m_{t\bar{t}}$ distribution and thus can be used for spin discrimination. Implementing the different spin combinations in Table 1 in CALCHEP [35] model files, we have performed parton-level simulations of the decay chain of a single \mathcal{Z} particle, obtaining Fig. 7.

For the fermion-scalar-fermion chain (scenarios vi–i), there are no spin correlations between the first and second step of the decay chain in Fig. 1, so the $m_{t\bar{t}}$ distribution follows the shape dictated by the pure phase-space kinematics. As a result, for this case, $d\Gamma/dm_{bbjj\ell}$ peaks at medium values of $m_{bbjj\ell}$.

In contrast, the scalar-fermion-scalar chain (scenario v–ii) displays maximal correlation effects in the $m_{t\bar{t}}$ distribution, since in this case angular momentum conservation demands alignment between the t and \bar{t} helicities. If the top and anti-top are produced with the same helicity (corresponding to the choices $a_L = b_R = 1$, $a_R = b_L = 0$ or $a_L = b_R = 0$, $a_R = b_L = 1$), then they are emitted preferentially in opposite directions, so that their spins add up to zero total angular momentum, as is necessary for the spin-0 initial \mathcal{Z} . As a result, in this case the invariant-mass distribution peaks at large values of $m_{bbjj\ell}$. On the other hand, for opposite helicities of the top and anti-top (that is, $a_L = b_L = 1$, $a_R = b_R = 0$ or $a_L = b_L = 0$, $a_R = b_R = 1$), they are emitted mostly in the same direction and thus the $m_{bbjj\ell}$ distribution peaks at small values.

If $m_X/m_Y \ll 1$, the results for the scalar-fermion-vector chain (scenario v–iii) are very similar, since the excitation of different spin states of the vector X is suppressed by m_X/m_Y [33]. On the other hand, for scenario viii–ii or viii–iii (vector-fermion-scalar or vector-fermion-vector), the spin-correlation effects in the $m_{t\bar{t}}$ distribution are slightly reduced, since angular momentum conservation now involves the helicity states of not only the t and \bar{t} but also the parent \mathcal{Z} . The correlation effects are even further washed out for scenario vii (fermion-vector-fermion), where both the initial \mathcal{Z} and final X have non-trivial spin states.

To study quantitatively how well one can distinguish between the different spin combinations, we have performed a χ^2 analysis for the binned $m_{bbjj\ell}$ distributions, using three bins*. The resulting χ^2 values are shown in Table 3 for an assumed signal sample of 857

*Larger numbers of bins do not yield additional information, but only reduce the discriminative power because of the increased number of degrees of freedom in the statistics.

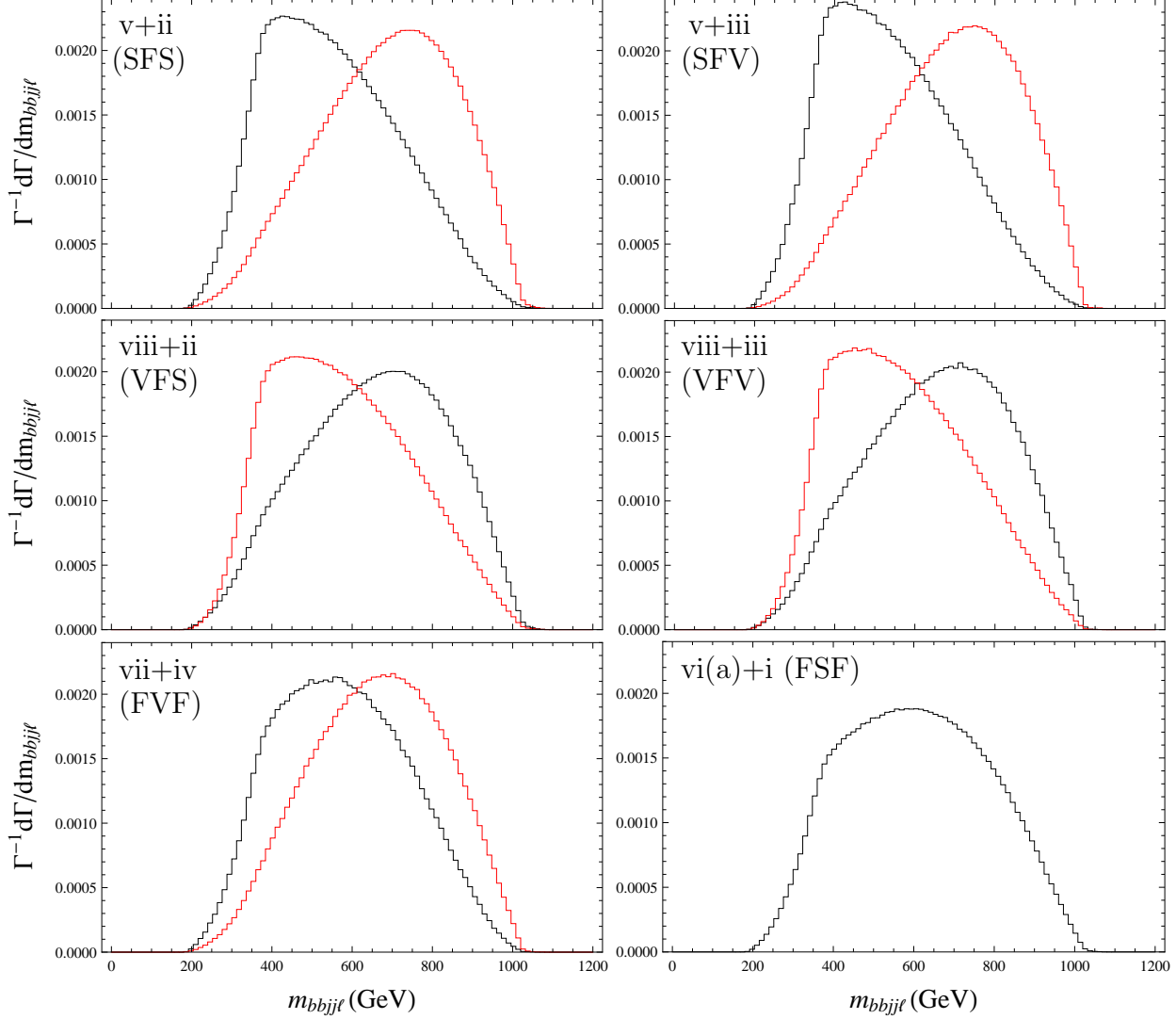


Figure 7: Parton-level invariant-mass distribution of the visible decay products, for the decay chain $\mathcal{Z} \rightarrow t\bar{Y}/\bar{t}Y \rightarrow t\bar{t}X$. The six panels show the results for the scenarios in Table 1, for the two coupling choices $a_L = 1, a_R = 0, b_L = 1, b_R = 0$ (black) and $a_L = 0, a_R = 1, b_L = 1, b_R = 0$ (red). Here, S, F, and V denote scalar, fermion, and vector particles, respectively, in the decay chain. The input mass parameters are $m_{\mathcal{Z}} = 1200$ GeV, $m_Y = 600$ GeV and $m_X = 100$ GeV. The distributions have been normalized to unity.

events. This event yield corresponds to production of Majorana fermion pairs $\mathcal{Z}\bar{\mathcal{Z}}$ with $m_{\mathcal{Z}} = 1200$ GeV at $\sqrt{s} = 14$ TeV with an integrated luminosity of 300 fb^{-1} . The number of events has been obtained using the simulation results of section 4 and the total cross section from Ref. [22].

As Table 3 shows, most pairs of spin combinations can be discriminated with high significance. An exception is pairs that differ only in the spin of the invisible X . Note that this analysis does not account for detector smearing effects, SM backgrounds, and combinatorial

	Spin combinations				
	SFV	VFS	VFV	FVF	FSF
SFS	1.3	10.3	10.6	2.4	5.3
SFV		11.4	11.8	3.5	6.4
VFS			0.35	9.6	4.7
VFV				9.6	4.8
FVF					3.6

Table 3: $\sqrt{\chi^2}$ values for the discrimination between pairs of different spin combinations, from a binned analysis of the invariant-mass distribution of the visible $t\bar{t}$ decay products. Here, S, F, and V denote scalar, fermion, and vector particles, respectively, in the decay chain. The results are based on 857 events for the following input mass and coupling parameters: $m_Z = 1200$ GeV, $m_Y = 600$ GeV, $m_X = 100$ GeV; $a_L = 1$, $a_R = 0$, $b_L = 1$, $b_R = 0$.

ambiguities in assigning the visible object in a given event to the decay chains of the Z and \bar{Z} .

5.3 Couplings

The observable invariant-mass distribution depends not only on the spin of the particles in the decay chain but also on the chiral structure of their couplings, that is, whether they are left- or right-handed (see Fig. 7). Recall that this effect is a manifestation of spin correlations between the two steps of the decay chain, and thus it is absent for a scalar Y . Furthermore, the invariant-mass distribution depends only the *relative* chirality between the first and second interactions in the decay chain, that is, whether Γ and Γ' in Table 1 have the same or opposite chirality.

Additional information on the couplings' chirality can be extracted from measurement of the top-quark polarization. The polarization can be determined from the angular distribution of the top-quark decay products. This method is particularly effective for large mass differences $m_Z - m_Y$ or $m_Y - m_X$, when the emitted top quarks are energetic, so their helicity is approximate preserved.

Following the analysis in Ref. [19], we study the distribution of the angle θ'_b of the b quark with respect to the top-quark boost direction in the top rest frame for the hadronically decaying top, t_h . Owing to the left-handedness of the weak decay $t \rightarrow W^+ b$, the b quark is emitted preferentially in the forward direction ($\cos \theta'_b > 0$) if the top quark is left-handed, and in the backward direction ($\cos \theta'_b < 0$) if the top quark is right-handed.

The resulting $\cos \theta'_b$ distributions are shown in Fig. 8, based on a parton-level simulation with CALCHEP. Since in general it is unknown whether the t_h emerged from the first or second step of the decay chain, the observable distributions correspond to an average of both. Consequently, when Γ and Γ' (specified by $a_{L,R}$ and $b_{L,R}$) have the same chirality, the $\cos \theta'_b$ distribution displays a strong polarization signal. On the other hand, if they have

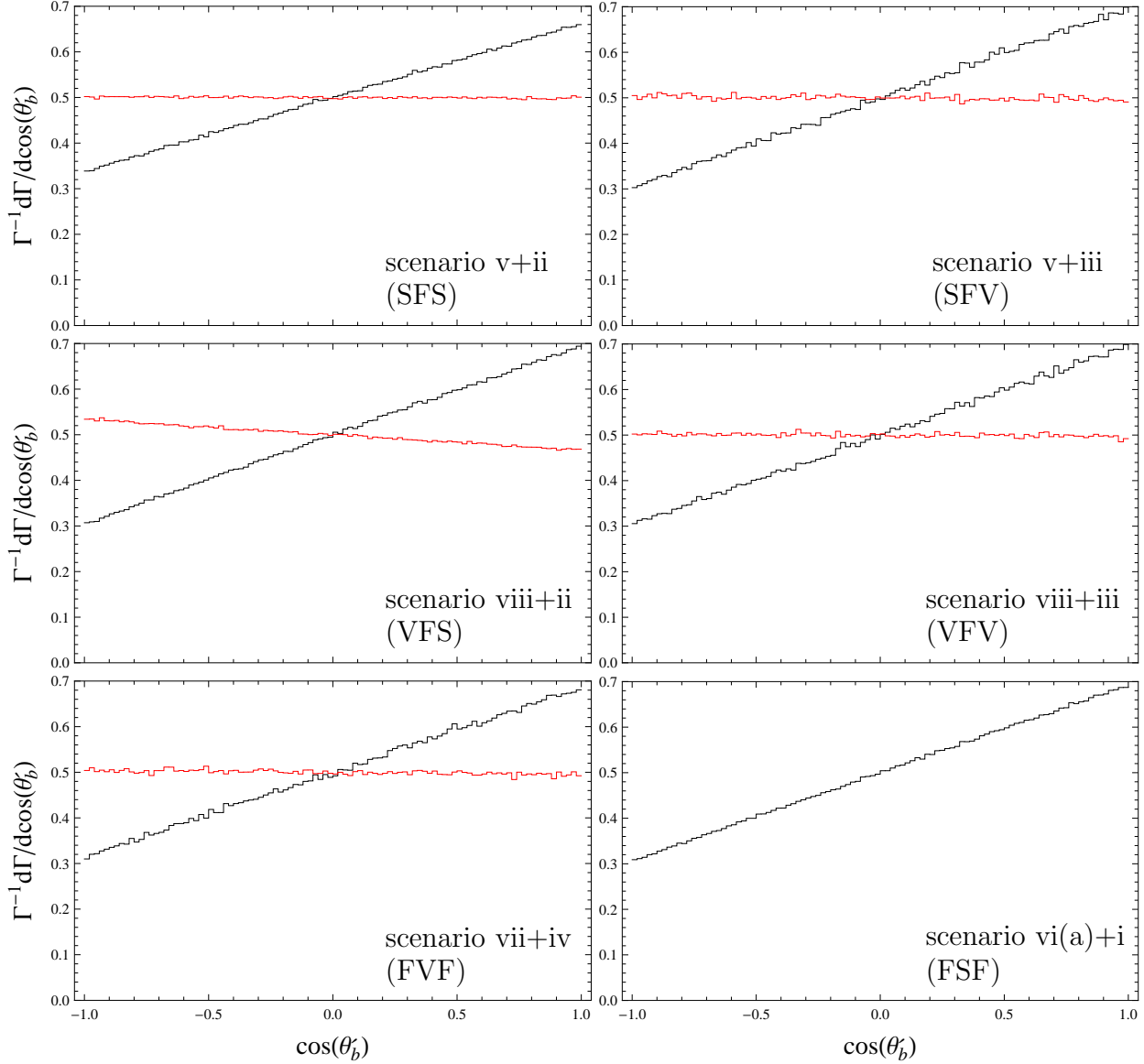


Figure 8: Parton-level angular distribution of the b -quark (jet) in the top-quark rest frame, for the decay chain $\mathcal{Z} \rightarrow t\bar{Y}/\bar{t}Y \rightarrow t\bar{t}X$. The six panels show the results for the scenarios in Table 1, for the two coupling choices $a_L = 1, a_R = 0, b_L = 1, b_R = 0$ (black) and $a_L = 0, a_R = 1, b_L = 1, b_R = 0$ (red). Here, S , F , and V denote scalar, fermion, and vector particles, respectively, in the decay chain. The input mass parameters are $m_{\mathcal{Z}} = 1200$ GeV, $m_Y = 600$ GeV and $m_X = 100$ GeV. The distributions have been normalized to unity.

opposite chirality, the top quarks from the two decay stages have opposite polarization, leading to an almost flat average $\cos \theta'_b$ distribution. Thus, the polarization analysis allows one to determine the chirality of the couplings regardless of the spins of X , Y or \mathcal{Z} .

5.4 Distinguishing between Majorana and Dirac Particles

In general, the color-octet \mathcal{Z} field may be self-conjugate or have distinct particles and antiparticles. In this subsection, we investigate whether these two possibilities can be distinguished experimentally at the LHC. For concreteness, we focus on a color octet with spin 1/2, corresponding to a Majorana or Dirac gluino in supersymmetric theories. In broad terms, there are two main approaches to distinguishing between self-conjugate and non-self-conjugate \mathcal{Z} particles:

1. One can take advantage of the fact that the production cross section for the Dirac case is larger than for the Majorana case by a factor of about 2; see Fig. 3 and Ref. [20]. However, a difficulty associated with this method is that the total cross section also depends strongly on the spin of the \mathcal{Z} , its branching fractions and its mass, which is challenging to measure precisely.

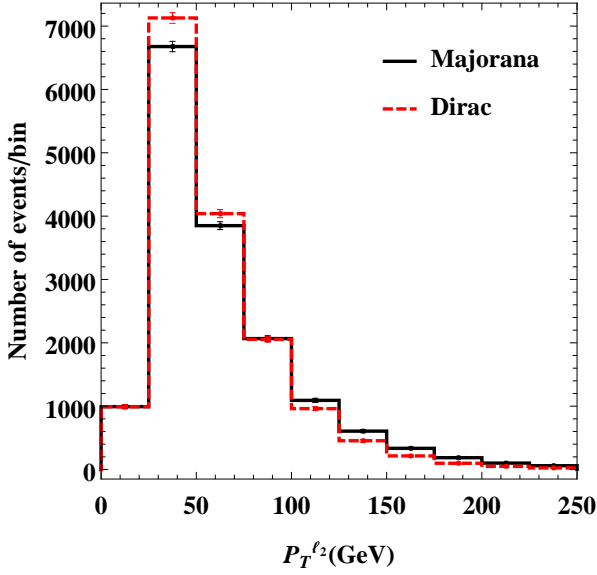
2. Alternatively, one can look for characteristics in the decay distributions of the $\mathcal{Z}\bar{\mathcal{Z}}$ pair. This is the approach we study in more detail here.

In the non-self-conjugate (Dirac) case, the \mathcal{Z} (gluino) decays into a Y (stop) and the $\bar{\mathcal{Z}}$ (anti-gluino) decays into a \bar{Y} (anti-stop). For the same-sign lepton signature, this means that one ℓ^+ has to come from the second decay step of the \mathcal{Z} and the other from the first decay step of the $\bar{\mathcal{Z}}$ (and vice versa for ℓ^-). In the self-conjugate (Majorana) case, in contrast, the two decay chains are independent, and therefore each of the two same-sign leptons can come from the same stage in its decay chain. Therefore, one expects the energy and $|\mathbf{p}_T|$ distributions of the two leptons to exhibit larger differences — in particular, the ℓ_2 will have a softer distribution — in the Dirac case than in the Majorana case.

The size of this effect depends crucially on kinematics. If $m_{\mathcal{Z}} - m_Y$ and $m_Y - m_X$ are approximately equal, the energy distributions of leptons from the first and second decay steps differ very little, so the Majorana–Dirac distinction is difficult to make. On the other hand, if $m_{\mathcal{Z}} - m_Y$ is significantly larger than $m_Y - m_X$, a lepton emitted from the second decay step $Y \rightarrow tX$ is on average softer than one from the first decay step $\mathcal{Z} \rightarrow \bar{t}Y$, so an attempted discrimination between Majorana and Dirac gluinos is promising. Even in this case, however, the effect is relatively small, so a large integrated luminosity will be needed for this analysis.

To study the effectiveness of this method, we have performed a Monte Carlo simulation of Majorana and Dirac gluino production at the LHC. The simulation of $\mathcal{Z}\mathcal{Z}$ (or $\mathcal{Z}\bar{\mathcal{Z}}$) pair production with the full decay chain, including top and W decays, with exact matrix elements is very difficult and requires large computational resources. Here, the following simplified approach has been taken: parton-level events for $pp \rightarrow t\bar{t}t\bar{t}XX$ have been generated with CALCHEP and passed to PYTHIA to perform the top-quark decays. This setup is computationally efficient but ignores the top-quark polarization. Therefore, we have to restrict ourselves to observables that are based only on kinematical features, such as the energy and $|\mathbf{p}_T|$ distributions proposed above.

A: $(m_Z, m_Y, m_X) = (1200, 600, 400)$ GeV



B: $(m_Z, m_Y, m_X) = (1200, 1000, 400)$ GeV

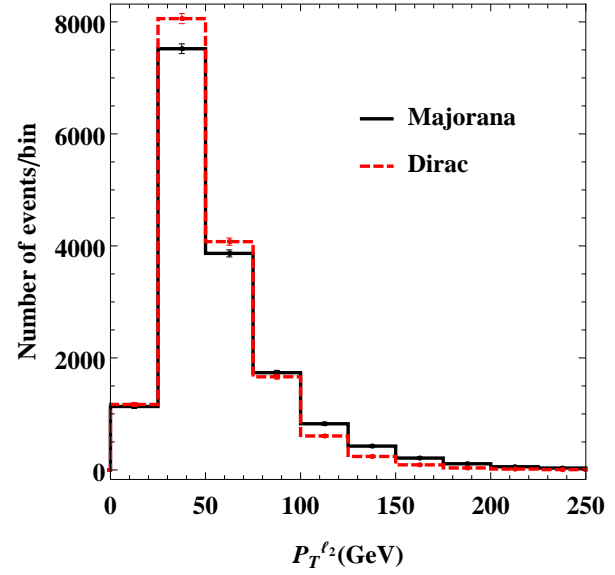


Figure 9: Hadron-level $|\mathbf{p}_{T,\ell_2}|$ distribution from pair production of Majorana fermion pairs ZZ (black solid) and Dirac fermion pairs $Z\bar{Z}$ (red dashed). The Dirac and Majorana cases correspond to scenarios vi(a)+i and vi(b)+i in Table 1, respectively. The chiral couplings have been fixed to $a_L = 1$, $a_R = 0$, $b_L = 1$, $b_R = 0$. The distributions have been normalized to the production cross section for Dirac octets after application of the selection cuts from section 4 at $\sqrt{s} = 14$ TeV and 3000 fb^{-1} ($N_{\text{ev}} = 16200$ and $N_{\text{ev}} = 15970$ for scenarios A and B, respectively), and the error bars indicate the statistical uncertainty.

As concrete examples, we have considered two choices for the mass spectrum:

$$\text{A : } m_Z = 1200 \text{ GeV}, \quad m_Y = 600 \text{ GeV}, \quad m_X = 400 \text{ GeV}, \quad (7)$$

$$\text{B : } m_Z = 1200 \text{ GeV}, \quad m_Y = 1000 \text{ GeV}, \quad m_X = 400 \text{ GeV}. \quad (8)$$

In scenario A, $m_Y - m_X \ll m_Z - m_Y$, whereas in scenario B, $m_Y - m_X \gg m_Z - m_Y$. For the numerical analysis, the same cuts as in section 4 have been applied. With the production cross section for Dirac $Z\bar{Z}$ pairs as the reference scenario, this choice produces an event yield of 16,200 for scenario A and 15,970 for scenario B at $\sqrt{s} = 14$ TeV, with an integrated luminosity of $3,000 \text{ fb}^{-1}$.

The resulting $|\mathbf{p}_{T,\ell_2}|$ distributions are shown in Fig. 9. The softer $|\mathbf{p}_T|$ spectrum of the second lepton in the Dirac case can be clearly seen in both scenarios. Performing a binned χ^2 analysis with three bins for each distribution, one obtains the following levels of statistical discrimination between Majorana and Dirac octets:

$$300 \text{ fb}^{-1} : \quad \text{A : } \sqrt{\chi^2} = 3.2, \quad \text{B : } \sqrt{\chi^2} = 4.1; \quad (9)$$

$$3000 \text{ fb}^{-1} : \quad \text{A : } \sqrt{\chi^2} = 10.1, \quad \text{B : } \sqrt{\chi^2} = 13.1. \quad (10)$$

Thus, a statistically significant exclusion of the scenario not realized in nature may be achievable at the full-energy run of the LHC.

6 Conclusions

In this paper, we have introduced a general categorization of new particles motivated by naturalness arguments, with different spin (0, 1/2, and 1) and color (octet \mathcal{Z} , triplet Y , and singlet X). There are four possible spin combinations permitting an interaction between the color triplet, singlet and top quark, and four possibilities for a coupling between the octet, triplet and top, as summarized in Table 1. The cross sections for the pair production of heavy color-octet particles, $\mathcal{Z}\bar{\mathcal{Z}}$, at LHC energies are shown in Fig. 3. These channels would lead to a spectacular signature of four top quarks and missing energy (see Eq. (1)), where it is assumed that the singlet X is stable and escapes detection. At the 14-TeV run of the LHC, this process is observable at the 5σ level up to gluon-partner masses of 1280 GeV for a scalar \mathcal{Z} , 1650 GeV for a fermionic \mathcal{Z} , and 1900 GeV for a vector \mathcal{Z} , provided that the missing particle X (the dark-matter candidate) is not too heavy, that is, $m_X \lesssim 300$ GeV. These results are summarized in Table 2.

If such a signal is discovered, understanding the underlying physics will require the determination of properties of the new particles. As a benchmark, we have taken the typical production rate of Majorana color-octet fermions with $\mathcal{O}(\text{TeV})$ mass at $\sqrt{s} = 14$ TeV with an integrated luminosity of 300 fb^{-1} . Through an analysis of the invariant-mass distribution of the visible decay products of top-quark pairs, most possible spin combinations can be discriminated from each other with high significance; χ^2 values are shown in Table 3. However, pairs that differ only in the spin of the invisible color singlet X are difficult to distinguish.

Furthermore, as Fig. 7 shows, the observable invariant-mass distribution is also affected by the chiral structure of the couplings of the particles in the decay chain, that is, whether they are left- or right-handed. Additional information on the couplings' chirality can be extracted from the top-quark polarization, which can be determined from the angular distribution of the top-quark decay products. The resulting $\cos\theta'_b$ distributions are shown in Fig. 8. The polarization analysis allows one to determine the chirality of the couplings independently of the spins of X , Y or \mathcal{Z} .

Finally, for the case of fermionic color-octet pair production, we have demonstrated that measurements at the LHC also allow us to distinguish whether these particles are Majorana or Dirac fermions, without recourse to the factor of 2 difference in the production cross sections. This is possible because, for a pair of Majorana particles, each can decay randomly and independently into a top quark or antiquark, whereas fermion number is conserved in the decays of a Dirac fermion. Consequently, depending on the mass hierarchy of the new \mathcal{Z} , Y and X particles, there can be distinct differences in the transverse-momentum distributions of the final-state decay products, as seen in Fig. 9.

We have shown that the full-energy run of the LHC will have a significantly expanded potential for searching for heavy color octets and triplets, as well as identifying their characteristic properties, which could lead to a new understanding of the naturalness of the electroweak scale. At a future 100-TeV VLHC, the mass coverage for a color-octet particle can be substantially extended, with a cross section many orders of magnitude greater than at the LHC, enabling the probing of \mathcal{Z} masses of the order of 10 TeV.

Acknowledgements

This project was supported in part by the National Science Foundation under grant PHY-1212635, by the US Department of Energy under grant Nos. DE-FG02-12ER41832 and DE-AC02-98CH10886, and by PITT PACC. Perimeter Institute is supported in part by the Government of Canada through Industry Canada and by the Province of Ontario through the Ministry of Research and Innovation.

References

- [1] R. Barbieri and G. F. Giudice, Nucl. Phys. B **306**, 63 (1988);
S. Dimopoulos and G. F. Giudice, Phys. Lett. B **357**, 573 (1995).
- [2] M. Papucci, J. T. Ruderman and A. Weiler, JHEP **1209**, 035 (2012).
- [3] See, for example, S. P. Martin, in “Perspectives on supersymmetry II,” ed. G. L. Kane, World Scientific, Singapore (2010), 1–153 [hep-ph/9709356].
- [4] See, for example, C. T. Hill and E. H. Simmons, Phys. Rept. **381**, 235 (2003) [Erratum-ibid. **390**, 553 (2004)].
- [5] C. T. Hill, Phys. Lett. B **266**, 419 (1991); C. T. Hill, Phys. Lett. B **345**, 483 (1995).
- [6] T. Appelquist, H. C. Cheng and B. A. Dobrescu, Phys. Rev. D **64**, 035002 (2001);
B. A. Dobrescu and E. Pontón, JHEP **0403**, 071 (2004);
G. Burdman, B. A. Dobrescu and E. Pontón, JHEP **0602**, 033 (2006).
- [7] G. Aad *et al.* [ATLAS Collaboration], ATLAS-CONF-2013-007.
- [8] G. Aad *et al.* [ATLAS Collaboration], arXiv:1404.2500 [hep-ex].
- [9] G. Aad *et al.* [ATLAS Collaboration], ATLAS-CONF-2013-061;
G. Aad *et al.* [ATLAS Collaboration], JHEP **1310**, 130 (2013).
- [10] S. Chatrchyan *et al.* [CMS Collaboration], JHEP **1401**, 163 (2014).
- [11] S. Chatrchyan *et al.* [CMS Collaboration], arXiv:1311.4937 [hep-ex];
S. Chatrchyan *et al.* [CMS Collaboration], CMS-PAS-SUS-13-008;
S. Chatrchyan *et al.* [CMS Collaboration], arXiv:1402.4770 [hep-ex].
- [12] G. L. Kane, E. Kuflik, R. Lu and L.-T. Wang, Phys. Rev. D **84**, 095004 (2011).
- [13] R. Essig, E. Izaguirre, J. Kaplan and J. G. Wacker, JHEP **1201**, 074 (2012);
Y. Kats, P. Meade, M. Reece and D. Shih, JHEP **1202**, 115 (2012).
- [14] T. Cohen, T. Golling, M. Hance, A. Henrichs, K. Howe, J. Loyal, S. Padhi and J. G. Wacker, JHEP **1404**, 117 (2014).

- [15] N. Polonsky and S. f. Su, Phys. Rev. D **63**, 035007 (2001).
- [16] P. J. Fox, A. E. Nelson and N. Weiner, JHEP **0208**, 035 (2002);
K. Benakli and C. Moura, in M. M. Nojiri *et al.*, arXiv:0802.3672 [hep-ph].
- [17] S. Y. Choi, M. Drees, J. Kalinowski, J. M. Kim, E. Pospenda and P. M. Zerwas, Phys. Lett. B **672**, 246 (2009); S. Y. Choi, D. Choudhury, A. Freitas, J. Kalinowski, J. M. Kim and P. M. Zerwas, JHEP **1008**, 025 (2010).
- [18] H. Cai, H.-C. Cheng and J. Terning, Phys. Rev. Lett. **101**, 171805 (2008).
- [19] C.-Y. Chen, A. Freitas, T. Han and K. S. M. Lee, JHEP **1211**, 124 (2012).
- [20] S. Y. Choi, M. Drees, A. Freitas and P. M. Zerwas, Phys. Rev. D **78**, 095007 (2008).
- [21] D. Gonçalves-Netto, D. Lopez-Val, K. Mawatari, T. Plehn and I. Wigmore, Phys. Rev. D **85**, 114024 (2012).
- [22] U. Langenfeld, S.-O. Moch and T. Pfoh, JHEP **1211**, 070 (2012).
- [23] C. Borschensky, M. Krmer, A. Kulesza, M. Mangano, S. Padhi, T. Plehn and X. Portell, arXiv:1407.5066 [hep-ph];
twiki.cern.ch/twiki/bin/view/LHCPhysics/SUSYCrossSections100TeVgluglu.
- [24] T. Sjöstrand, S. Mrenna and P. Z. Skands, JHEP **0605**, 026 (2006).
- [25] J. M. Campbell and R. K. Ellis, JHEP **1207**, 052 (2012).
- [26] M. V. Garzelli, A. Kardos, C. G. Papadopoulos and Z. Trocsanyi, JHEP **1211**, 056 (2012).
- [27] J. M. Campbell, R. K. Ellis and C. Williams, JHEP **1107**, 018 (2011).
- [28] C. G. Lester and D. J. Summers, Phys. Lett. B **463**, 99 (1999).
- [29] For recent reviews, see
sect. 4 in A. J. Barr and C. G. Lester, J. Phys. G **37**, 123001 (2010), and refs. therein;
sect. X in A. J. Barr, T. J. Khoo, P. Konar, K. Kong, C. G. Lester, K. T. Matchev and M. Park, Phys. Rev. D **84**, 095031 (2011), and refs. therein.
- [30] H.-C. Cheng, J. F. Gunion, Z. Han, G. Marandella and B. McElrath, JHEP **0712**, 076 (2007).
- [31] D. E. Kaplan, K. Rehermann, M. D. Schwartz and B. Tweedie, Phys. Rev. Lett. **101**, 142001 (2008);
T. Plehn, M. Spannowsky, M. Takeuchi and D. Zerwas, JHEP **1010**, 078 (2010).
- [32] J. M. Smillie and B. R. Webber, JHEP **0510**, 069 (2005).

- [33] C. Athanasiou, C. G. Lester, J. M. Smillie and B. R. Webber, JHEP **0608**, 055 (2006).
- [34] C. Kilic, L.-T. Wang and I. Yavin, JHEP **0705**, 052 (2007);
M. Burns, K. Kong, K. T. Matchev and M. Park, JHEP **0810**, 081 (2008).
- [35] A. Belyaev, N. D. Christensen and A. Pukhov, Comput. Phys. Commun. **184**, 1729 (2013).